

# Early Source Characterization of Large Earthquakes Using *W* Phase and Prompt Elastogravity Signals

Kévin Juhel<sup>1,2</sup> , Zacharie Duputel<sup>3,4</sup> , Luis Rivera<sup>5</sup> , and Martin Vallée<sup>3</sup> 

## Abstract

In the minutes following a large earthquake, robust characterization of the seismic rupture can be obtained from full wavefield records at local distances or from early signals recorded by regional broadband seismometers. We focus here on the latter configuration, and evaluate the individual and joint performances of the early low-frequency elastic phases (*W* phase) and the recently discovered prompt elastogravity signals (PEGS). The 2011  $M_w$  9.1 Tohoku–Oki earthquake is a natural target for this evaluation, because the high quality of global and regional networks enabled to gather the best PEGS data set so far. We first confirm that the well-established *W*-phase method, using records from global seismological networks, is able to provide a reliable centroid moment tensor solution 22 min after the earthquake origin time. Using regional stations, an accurate *W*-phase solution can be obtained more rapidly, down to 10 min after origin time. On the other hand, a PEGS-based source inversion can provide even earlier, starting 3 min after origin time, a lower bound of the seismic moment ( $M_w$  8.6) and constraints on the focal mechanism type. However, relying solely on PEGS introduces uncertainties caused by the hindering seismic noise and trade-offs between source parameters that limit the accuracy of source determination. We show that incorporating even a few early *W* phase signals to the PEGS data set reduces these uncertainties. Using more complete *W* phase and PEGS data sets available 5 min after origin time enables to converge towards a result close to the Global Centroid Moment Tensor solution.

**Cite this article as** Juhel, K., Z. Duputel, L. Rivera, and M. Vallée (2023). Early Source Characterization of Large Earthquakes Using *W* Phase and Prompt Elastogravity Signals, *Seismol. Res. Lett.* **XX**, 1–11, doi: [10.1785/0220230195](https://doi.org/10.1785/0220230195).





[Supplemental Material](#)

## Introduction

Large earthquakes pose a dual challenge in terms of their early and quantitative characterization. In particular, for offshore earthquakes, the rapid determination of their moment magnitude and their focal mechanism is the key for tsunami warning purposes. In theory, the use of local seismic and/or geodetic data enables to characterize the earthquake source shortly after the end of the rupture. Several methods using strong-motion data (e.g., Delouis, 2014) or geodetic data (e.g., Colombelli *et al.*, 2013; Minson *et al.*, 2014) have been developed in this respect. However, such a near-real-time determination is challenging for a very large earthquake, because the observed waveforms are dependent both on the rupture history and on the (usually not well known) detailed fault geometry. Besides this difficulty, waveform fitting may be biased toward the modeling of local slip features that carry only indirect information on the overall moment magnitude.

In this context, data recorded at distances significantly larger than the rupture dimension are beneficial, because the earthquake can be modeled at low frequency as a simple point source. However, due to the increased travel times, the

use of elastic waves recorded at such distances has the obvious drawback to delay the time of possible source characterization. The recently observed and modeled prompt elastogravity signals (PEGS, Vallée *et al.*, 2017; Vallée and Juhel, 2019), which can be measured between origin time and *P*-wave arrivals, associate the two advantages of far and early observation. Their potential for instantaneous magnitude determination has been further characterized by Licciardi *et al.* (2022). The study of Zhang *et al.* (2020) has both provided an efficient modeling of the PEGS Green's functions and the first moment tensor inversion using these data.

1. Université Côte d'Azur, IRD, CNRS, Observatoire de la Côte d'Azur, Géoazur, Sophia Antipolis, France,  <https://orcid.org/0000-0003-0881-6904> (KJ);
2. Laboratoire de Planétologie et Géosciences, Nantes Université, CNRS UMR 6112, France;  <https://orcid.org/0000-0002-8809-451X> (ZD);  <https://orcid.org/0000-0001-8049-4634> (MV);
4. Observatoire Volcanologique du Piton de la Fournaise, Institut de physique du globe de Paris, La Réunion, France;
5. Institut Terre et Environnement de Strasbourg (ITES), Université de Strasbourg, CNRS, Strasbourg Cedex, France,  <https://orcid.org/0000-0002-0726-5445> (LR)

\*Corresponding author: [kjuhel@geoazur.unice.fr](mailto:kjuhel@geoazur.unice.fr)

© Seismological Society of America

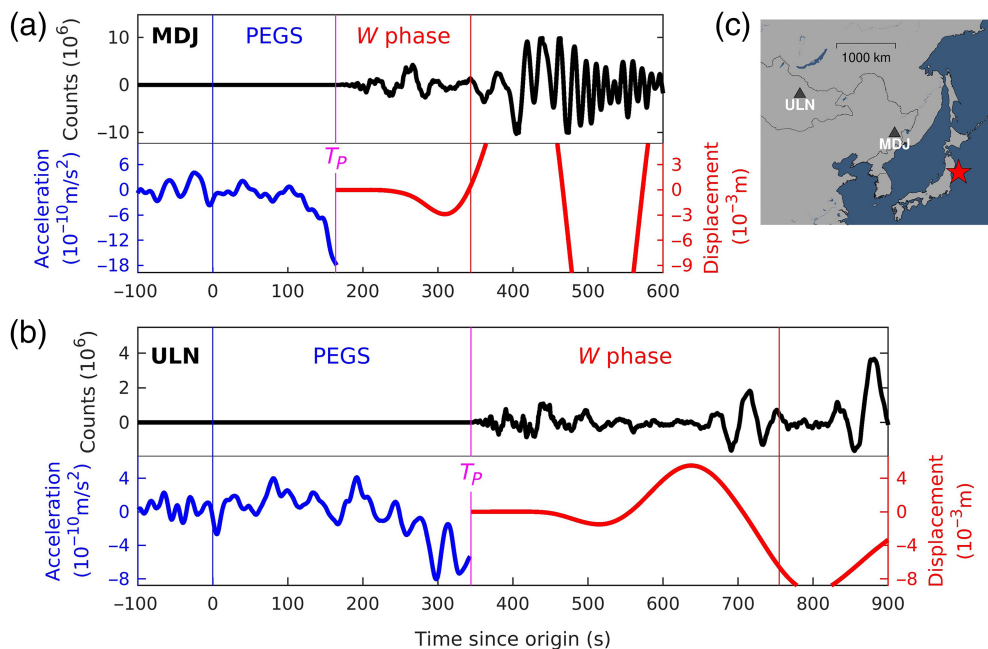


**Figure 1.** Prompt elastogravity signal (PEGS) and low-frequency elastic phase (*W*-phase) recorded at MDJ and ULN stations, during and after the 2011 Tohoku–Oki earthquake. (a) Vertical signal recorded at MDJ (IC.MDJ.00 STS-1 sensor, epicentral distance  $\Delta = 11.6^\circ$ ). The top subfigure shows in black the raw signal, which is clipped by surface waves at times later than  $\approx 400$  s.  $T_P$  time (vertical magenta line) is both the end of the PEGS time window (which begins at origin time) and the beginning of the *W*-phase time window (which ends at a distance-dependent time marked by the vertical red line). The bottom subfigure shows both the data types, because they are used in this study: for PEGS (blue), signal is converted to acceleration and filtered in the (0.002–0.03 Hz) frequency range; for *W* phase (red), signal is converted to displacement and filtered in the (0.001–0.005 Hz) frequency range. (b) Same as panel (a) for ULN station (IU.ULN.00 STS-1 sensor,  $\Delta = 27.4^\circ$ ). (c) Location of MDJ and ULN stations with respect to the epicenter of the 2011 Tohoku–Oki earthquake (red star). For horizontal components (not shown), the same data processing is applied, but only *W*-phase signals are considered, as the lower signal-to-noise ratio (SNR) of these components prevents from using the associated PEGS. The color version of this figure is available only in the electronic edition.

However, moment tensor inversion using PEGS alone are expected to suffer from uncertainties, because PEGS were clearly observed only on the vertical channels of high-quality broadband sensors (mostly STS-1s belonging to the Global Seismographic Network [GSN], GEOSCOPE, or F-net networks) and because the pre-*P* time can be short compared with the earthquake duration. As mentioned by Zhang *et al.* (2020), an interesting perspective, which will be evaluated in the present study, is to associate PEGS with the early elastic waves recorded at regional broadband stations.

Early low-frequency elastic phases have been coined *W* phase by Kanamori (1993), and *W* phase has been extensively used for moment tensor inversion since the study of Kanamori and Rivera (2008). Thanks to the low-frequency band (0.001–0.005 Hz) used in the inversion, *W* phase is little sensitive (as PEGS) to the Earth structure and to the details of the source process. Therefore, *W* phase inversion is well

suitable for the quantitative determination of the first-order source parameters, even for the largest earthquakes.

In this study, we first propose to document the performances and individual merits of each of the data types (*W* phase and PEGS) for the source determination of the 2011 Tohoku–Oki earthquake. This earthquake is indeed the event that generated the best PEGS data set so far, and the high-quality stations of the global and F-net seismic networks provide good records of the *W* phase at regional and teleseismic distances. The other PEGS case studies reported in Vallée and Juhel (2019) either suffered from a less effective seismic source for PEGS generation (lower magnitude) or a suboptimal recording environment (less instrumented area and noisier time series), which would prevent us from conducting a robust enough source inversion based on PEGS. We show in Figure 1 an illustration of the *W* phase and PEGS records during the Tohoku–Oki earthquake, at MDJ and ULN stations from the GSN

(Scripps Institution of Oceanography, 1986; Albuquerque Seismological Laboratory/U.S. Geological Survey [USGS], 2014). This figure highlights how PEGS and *W* phase make use of contiguous time windows, recorded at early times after the earthquake origin. In a second step, we will explore to which extent the joint use of PEGS with regional *W*-phase signals can lead to both rapid and reliable source determination of the Tohoku–Oki earthquake.

## Rapid Characterization of the 2011 Tohoku–Oki Earthquake Using the *W* Phase

The *W* phase is a long-period signal (100–1000 s) that is visible for large earthquakes between the *P* wave and the surface waves. According to normal-mode theory, this phase can be described as the superposition of long-period normal-mode overtones (Kanamori, 1993). The *W* phase is particularly suited for rapid source characterization of large earthquakes

for three main reasons. First, because it corresponds to very long periods and very long wavelengths, it can be modeled using point-source parameters even for great earthquakes ( $M_w > 8.0$ ). This is particularly useful to obtain an overall description of the source shortly after the earthquake origin time, when very little information about the rupture is available. Second, the  $W$  phase is very little affected by 3D Earth heterogeneities, because most of its energy propagates in the mantle, where lateral structure variations are relatively small (Kanamori and Rivera, 2008; Morales-Yáñez *et al.*, 2020). Finally, the  $W$  phase ends before surface-wave arrivals, making it quickly available and not prone to clipping issues that are often encountered for large earthquakes (Fig. 1).

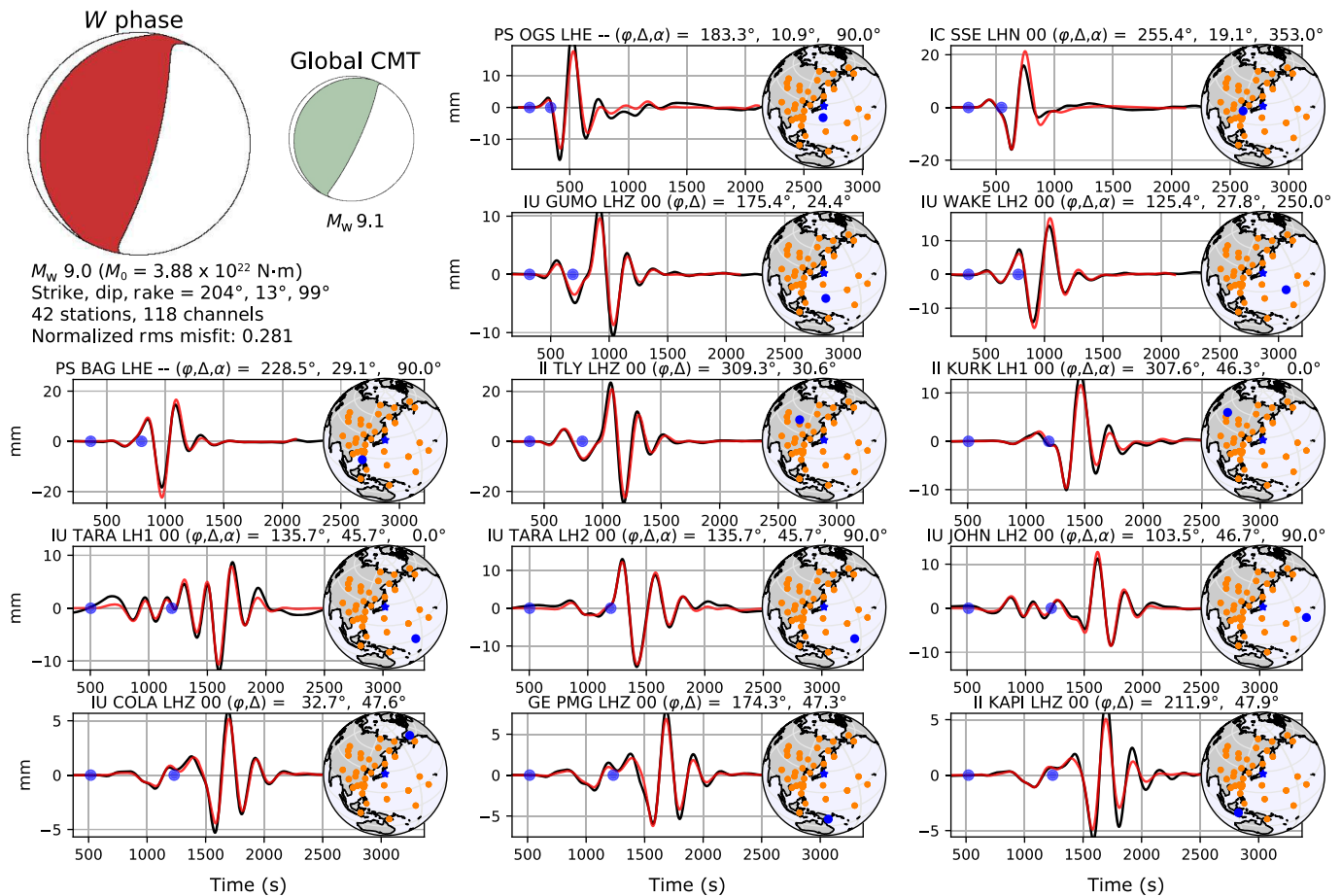
Taking advantage of these properties, Kanamori and Rivera (2008) proposed to use the  $W$  phase to accelerate the determination of the source of large earthquakes. They developed a simple and robust source inversion algorithm to estimate the centroid moment tensor parameters (i.e., the moment tensor elements along with the centroid location in time and space) between 20 and 35 min after the earthquake origin time. This idea came in a timely manner, a few years after the 2004 Sumatra–Andaman earthquake ( $M_w$  9.1) and the 2006 Java tsunami earthquake ( $M_w$  7.7), which caused damaging tsunamis with arrival times to the nearest coasts ranging from 25 min to 1 hr. The algorithm was then tested extensively and extended to moderate-size earthquakes (down to  $M_w$  5.8; Duputel *et al.*, 2012). It is now implemented in various operational and warning centers, including for example the National Earthquake Information Center-USGS (Hayes *et al.*, 2009), the Pacific Tsunami Warning Center (PTWC-National Oceanic and Atmospheric Administration; Wang *et al.*, 2012), and the Polynesian Center for Tsunami Prevention-Commissariat à l'énergie atomique et aux énergies alternatives, France.

The robustness of  $W$ -phase solutions is illustrated in Figure 2 for the 2011 Tohoku–Oki earthquake ( $M_w$  9.1 according to Global Centroid Moment Tensor [Global CMT]). Here, we use broadband seismological records from global seismological networks up to the maximum epicentral distance  $\Delta = 50^\circ$ . The data are time-windowed between the  $P$  arrival time  $T_p$  and  $T_p + 15 \times \Delta[s/^\circ]$ , and pass-band filtered between 1 and 5 mHz, which is the typical frequency band used to characterize  $M_w \geq 8.0$  earthquakes using the  $W$  phase. In real-time conditions, this solution would be obtained 22 min after the origin time. We use the preliminary hypocenter determination released 9.7 min after the origin time in the first PTWC bulletin (latitude =  $38.0^\circ$ , longitude =  $142.9^\circ$ , depth = 10 km; Hayes *et al.*, 2011) for data time-windowing (i.e., to estimate  $T_p$ ) and as an initial centroid location. An initial centroid time-shift  $\tau_c$  and half-duration  $h_d$  are estimated from the scaling law  $\tau_c = h_d = 1.2 \cdot 10^{-8} M_0^{1/3}$  ( $M_0$  is given in dyne-cm and the time in s), where the scalar seismic moment  $M_0 = 10^{1.5 M_{wp} + 16.1}$  is defined from the PTWC preliminary magnitude  $M_{wp}$  7.9. Following the approach described in Duputel *et al.* (2012), these

parameters are used to conduct a first data screening and moment tensor inversion. This preliminary solution is then improved by conducting a grid search to find an optimum centroid timing ( $\tau_c = 68$  s) and location (latitude =  $37.70^\circ$ , longitude =  $143.28^\circ$ , depth = 19.5 km). A final inversion is conducted at this optimum centroid location assuming that the half-duration is equal to the centroid time shift (i.e.,  $\tau_c = h_d$ ). The resulting solution shown in Figure 2 is in good agreement with the Global CMT solution, even if the  $W$ -phase solution is obtained totally automatically (e.g., without any manual data screening or windowing) assuming a simple spherical Earth model (i.e., preliminary reference Earth model [PREM], Dziewonski and Anderson, 1981). The agreement between observations and predicted waveforms is also remarkably good even for later surface-wave arrivals that are not included in the inversion. Details about  $W$ -phase solutions obtained in real time after the 2011 Tohoku–Oki earthquake can be found in Duputel *et al.* (2011) and Hayes *et al.* (2011).

To further accelerate the availability of  $W$ -phase solutions, later developments have focused on waveforms available at regional distances. An example of such application is shown in Figure 3 for the Tohoku–Oki earthquake using the high-gain broadband F-net seismometers (LH channels) within  $20^\circ$  of epicentral distance. Because the standard  $W$ -phase time window is too short at very close distances, regional solutions are obtained by imposing the minimal time-window duration of 180 s starting at the  $P$ -arrival time. Data screening is performed automatically as for the global solution, and we use the same preliminary hypocenter and magnitude (from the PTWC bulletin issued 9.7 min after origin time). To damp the effect of source finiteness and mitigate clipping issues at short epicentral distances, we also mask out stations within  $\Delta < 3.5^\circ$ . We note instrumental clipping issues that occur at several stations after the time window used for source inversion. The obtained results shown in Figure 3 are in good agreement with the solution obtained at global scale (Fig. 2). This regional solution can be obtained within 10 min after the origin time in real-time scenarios, which is a significant improvement compared with the typical 20–40 min timeframe required for global  $W$ -phase inversion results (Duputel *et al.*, 2011). Although these results are very encouraging, it is important to point out that such an application is only possible in well-instrumented regions with good-quality broadband networks. In addition, for extremely large earthquakes with rupture duration longer than 180 s, such as the 2004 Sumatra–Andaman earthquake, the regional  $W$ -phase inversion may not be able to capture the entire rupture process. Regional instances of the  $W$ -phase source inversion algorithm now operate routinely at several regional centers like, for example, the Chilean Centro Sismológico Nacional-UCHile, Chile, Riquelme *et al.* (2016), the Servicio Sismológico Nacional-Universidad Nacional Autónoma de México, Mexico, or the southern California Earthquake Data Center.

Global solution (LH channels) - Origin time + 22 min ( $\Delta < 50^\circ$ )



### Early Characterization of the 2011 Tohoku-Oki Earthquake Using Pegs

PEGS are long-period signals measurable between the earthquake origin time and *P*-wave arrival time at the sensor location (Fig. 1). The recorded signal can be seen as the difference between a direct gravity perturbation and the gravity-induced inertial response of the medium surrounding the sensor (Vallée *et al.*, 2017). Pegs are usually measured on (very-) broadband sensors in the 2–30 mHz frequency range, to remove hindering effects from background seismic noise and unreliable very-low-frequency instrumental artifacts. Pegs observations have been documented on six earthquakes in different tectonic settings (either subduction, strike-slip, or deep dip-slip earthquakes), including the 2011 Tohoku-Oki earthquake (Vallée and Juhel, 2019).

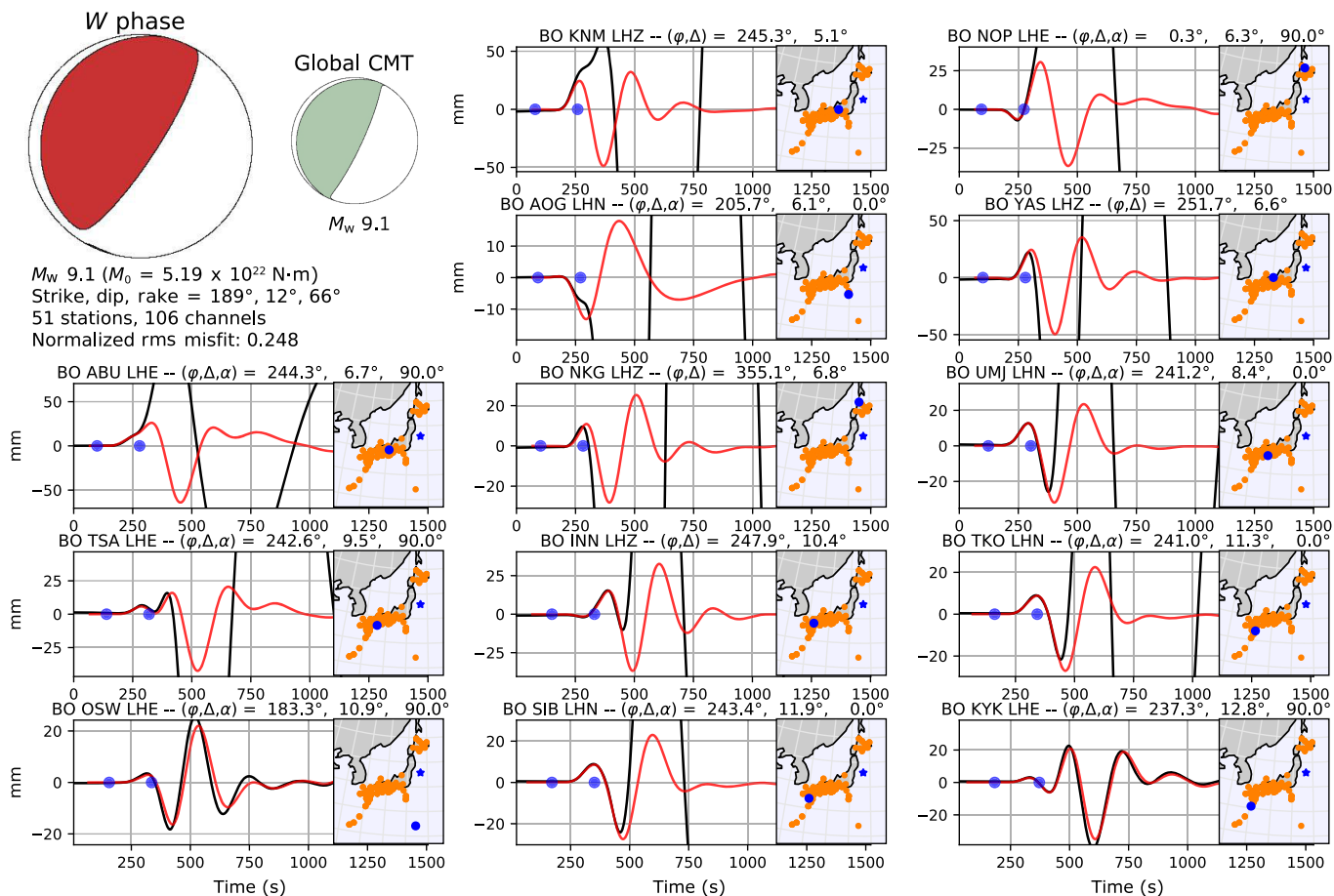
PEGS share several properties with *W* phase that make Pegs a promising observable for the monitoring and characterization of large earthquakes. First, Pegs are sensitive to first-order source parameters, and several studies have shown a good agreement between recorded waveforms and Pegs synthetics based on a point-source approximation and a simple 1D Earth model (Juhel *et al.*, 2019; Vallée and Juhel, 2019; Zhang *et al.*, 2020). Second, a Pegs data set can be gathered very quickly, because

**Figure 2.** *W*-phase source inversion result for the 2011  $M_w$  9.1 Tohoku-Oki earthquake using global seismological data within  $\Delta < 50^\circ$ . In real-time conditions, this solution would be obtained  $\sim 22$  min after the earthquake origin time. *W*-phase and Global Centroid Moment Tensor (Global CMT) solutions are shown on the top left corner. The other subplots are examples of data (black) and predicted waveforms (red) computed from the *W*-phase Centroid Moment Tensor (CMT) solution. The part of the signal used for inversion is delimited with blue dots. The station azimuth ( $\phi$ ) and epicentral distance ( $\Delta$ ) are indicated on top of each trace (the station location is also shown with a blue circle in the map inset). The azimuth ( $\alpha$ ) of horizontal component channels is also displayed. The orange circles in the right map insets show the global distribution of stations used for the inversion, and the blue star indicates the earthquake source location. The color version of this figure is available only in the electronic edition.

the latest signal becomes available as soon as the *P*-wave arrives at the farthest broadband sensor in which the signal is measurable. Practically, with respect to origin time, the Pegs data set becomes usable after several tens of seconds and is complete after several hundreds of seconds. Finally, because Pegs are very-low-amplitude signals (no more than a few  $\text{nm/s}^2$ , even for the largest events), they are not prone to clipping.



Regional solution (FNET, LH channels) - Origin time + 10 min ( $\Delta < 20^\circ$ )



Zhang *et al.* (2020) estimated the Tohoku–Oki earthquake source parameters (moment magnitude, rupture duration, and focal mechanism) based on the minimization of the misfit between PEGS synthetics and recordings from the 11 good-quality stations selected by Vallée *et al.* (2017). Kimura *et al.* (2021) later used records from Hi-net tiltmeters and F-net broadband seismometers. We select vertical recordings of broadband seismometers from the GSN and GEOSCOPE (Institut de physique du globe de Paris [IPGP] and École et Observatoire des Sciences de la Terre de Strasbourg [EOST], 1982) global networks, and from regional (F-net and the temporary Northeast China Extended Seismic Array [YP]) networks, at distances up to 4000 km from the earthquake. To ensure the stability of PEGS computations, we only consider sensors for which the  $P$ -wave arrival time is larger than 45 s. We also remove the noisiest sensors in which PEGS are unlikely to be resolved, that is, we only keep channels for which the standard deviation in the 600 s-long time-window preceding the event is below  $1 \text{ nm/s}^2$ . Such criteria eventually led to the selection of 96 channels (see their locations in Fig. 4), which will be progressively integrated into the data set. A selection of channels in the PEGS data set is listed in Table 1, corresponding to the best-quality stations and stations with the highest PEGS observation potential. The high signal-to-noise

**Figure 3.**  $W$ -phase source inversion result for the 2011  $M_w$  9.1 Tohoku–Oki earthquake using F-net data within  $\Delta < 20^\circ$ . In real-time conditions, this solution would be obtained  $\sim 10$  min after the earthquake origin time.  $W$ -phase regional and Global CMT solutions are shown on the top left corner. The other subplots are examples of data (black) and predicted waveforms (red) computed from the  $W$ -phase CMT solution. The part of the signal used for inversion is delimited with blue dots. The station azimuth ( $\phi$ ) and epicentral distance ( $\Delta$ ) are indicated on top of each trace (the station location is also shown with a blue circle in the map inset). The azimuth ( $\alpha$ ) of horizontal component channels is also displayed. The orange circles in the right map insets show the overall distribution of stations used for the inversion, and the blue star indicates the earthquake source location. The color version of this figure is available only in the electronic edition.

ratio (SNR) of stations from the global networks located at regional distances (such as IC.MDJ, IU.INCN, and IC.BJT) emphasizes their critical importance in PEGS-based source inversions, as already noted by Vallée *et al.* (2017).

To infer the focal mechanism, we choose to describe the earthquake as a pure deviatoric seismic source and use as basis five elementary moment tensors:  $m_{r\theta}$ ,  $m_{r\phi}$ ,  $m_{\theta\phi}$ ,  $m_{rr} - m_{\theta\theta}$ , and  $m_{\theta\theta} - m_{\phi\phi}$  (see, e.g., Kikuchi and Kanamori, 1991). We compute

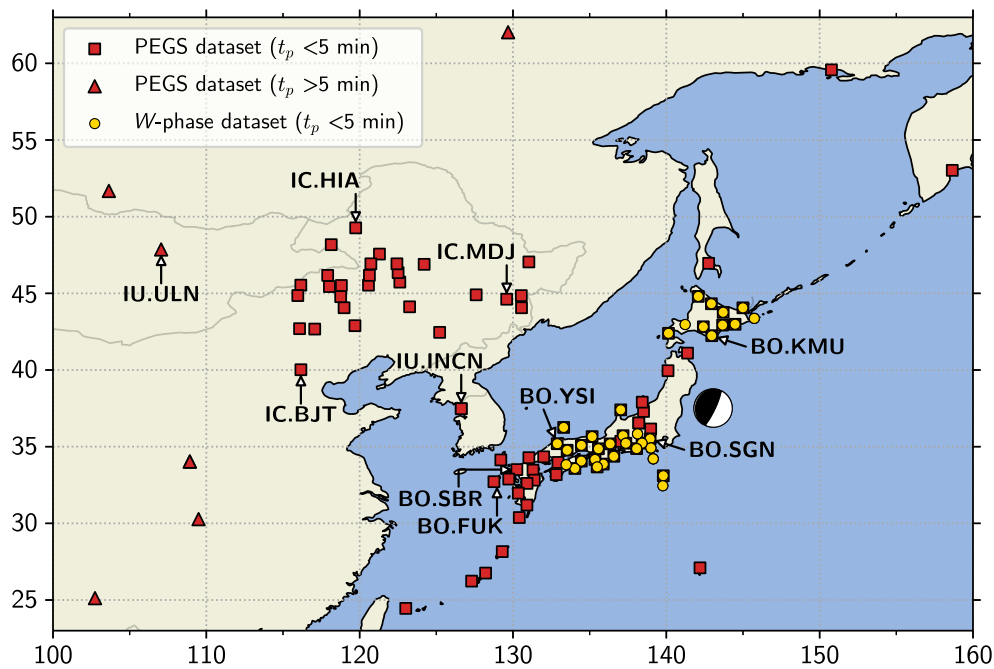


**Figure 4.** Location of the broadband stations used for the PEGS-based inversion, and for the joint inversion of PEGS and *W*-phase signals. For the joint inversion, all the data available within 5 min after origin time are used. These data are either *W*-phase signals from stations in Japan located at epicentral distances  $\Delta < 8.3^\circ$  (yellow dots) or PEGS from stations with  $\Delta < 22.5^\circ$  (red squares). For the PEGS-based inversion, all PEGS are used, including signals recorded by stations with  $\Delta > 22.5^\circ$  (red triangles). The focal mechanism shows the Global CMT solution for the 2011 Tohoku–Oki earthquake. Stations named on the map are either the ones explicitly mentioned in the [Early Characterization of the 2011 Tohoku–Oki Earthquake using PEGS](#) and [Joint Use of PEGS and \*W\* phase for Early Source Characterization](#) sections or those with the best PEGS observation potential (see Table 1). The color version of this figure is available only in the electronic edition.

the PEGS Green’s functions corresponding to these five elementary sources at each sensor location using the QSSP algorithm (Wang *et al.*, 2017; Zhang *et al.*, 2020), inside a PREM model (Dziewonski and Anderson, 1981) for which the upper layers have been modified to match the Japanese crustal environment. We consider the point-source location to be known and use Global CMT centroid location (latitude =  $37.52^\circ$ , longitude =  $143.05^\circ$ , depth = 20.0 km). Such an assumption may be regarded as acceptable, because Zhang *et al.* (2020) showed that PEGS computations are little sensitive to source depth (as long as it is within a few tens of kilometers). Similarly, the smooth variations of PEGS (Vallée and Juhel, 2019; Zhang *et al.*, 2020) and the long observation distances make them little sensitive to any epicentral location within the rupture zone of the Tohoku–Oki earthquake. The weak sensitivity of the inversion results to different prescribed locations (up to 150 km away from the Global CMT centroid) is illustrated in Figure S1. This figure also shows that, in the case of the Tohoku–Oki earthquake, the use of first-arrival epicentral locations (which can be known in near-real time) provides similar results.

Both recorded data and PEGS Green’s functions are cut at *P*-wave arrival time, and band-pass filtered between 2.0 mHz (high-

pass Butterworth causal filter with two poles) and 30.0 mHz (low-pass Butterworth filter with six poles). Each trace is later normalized by an estimate of the noise level at each station, that is, the standard deviation of each record in the 600 s long time window preceding the event. Such a strategy avoids that the noisiest stations jeopardize the following inversions and ensures a driving role for good-quality stations (including several regional stations from global networks, located close to the optimal locations for PEGS detection, see Table 1).

We seek the least-squares solution  $\mathbf{m}$  in the time domain that minimizes the L2-norm  $\|\mathbf{G}\mathbf{m} - \mathbf{y}\|$ , in which  $\mathbf{y}$  is the data vector, and  $\mathbf{G}$  is the five-column matrix of PEGS Green’s functions (one for  $m_{r\theta}$ , one for  $m_{r\phi}$  and so on). The vector solution  $\mathbf{m}$  of the linear inversion gives the inverted focal mechanism, and its norm leads to the predicted scalar seismic moment. To

overcome the nonlinearity associated to the search of source time function (STF) parameters (source half-duration  $h_d$  and centroid time shift  $\tau_c$ ), we explore an exhaustive set of triangular-shaped STFs and loop over all the combinations of  $h_d$  and  $\tau_c$  values (with  $h_d \leq \tau_c$ ), ranging from 5 to 200 s, every 5 s. The selection of the  $(h_d, \tau_c)$  couple leading to the solution presented in Figure 5 is further described in the supplemental material.

To assess the performance of PEGS-based inversions for the determination of earthquake source parameters, we use the geometrical similarity  $\alpha$  (see equation 4 of Rivera and Kanamori, 2014), which measures the difference of radiation patterns between two normalized seismic moment tensors. A geometrical similarity close to 0 indicates opposite focal mechanisms, whereas focal mechanisms are identical when  $\alpha = 1$ . We compare the obtained PEGS-based solutions with the Global CMT solution for the 2011 Tohoku–Oki earthquake. We see in Figure 5 that  $\alpha$  exceeds 0.9 three minutes after onset time, but the agreement with the Global CMT solution is then temporarily degraded by the addition of later channels. The geometrical similarity again reaches values above 0.9 for the latest times between  $t = t_0 + 6$  min and  $t = t_0 + 7$  min, in which the inverted moment magnitude  $M_w$  is in the (8.8–9.0) range.

TABLE 1

**Selection of Stations Inside the PEGS Data Set**

Station Code	Noise Level (in nm/s <sup>2</sup> )	Station Code	SNR
BO.SHR	0.12	IC.MDJ.00	9.5
BO.FUK	0.15	IU.INCN.10	8.4
BO.SBR	0.15	IC.BJT.00	7.8
BO.URH	0.15	BO.SBR	7.3
BO.GJM	0.16	BO.FUK	7.0
BO.SGN	0.16	BO.YSI	5.7
IC.BJT.00	0.16	IC.HIA.00	5.4
IC.XAN.00	0.16	BO.INN	4.8
BO.KNP	0.17	BO.WJM	4.7
BO.NOP	0.17	YP.NE93	4.5
BO.WJM	0.17	YP.NE12	4.5
G.INU.00	0.17	BO.ISI	4.5
IU.MAJO.10	0.17	BO.NRW	4.4
IU.ULN.00	0.17	BO.IZH	4.4
BO.KNM	0.18	IU.ULN.00	4.2
IC.KMI.00	0.18	IC.XAN.00	4.1
IC.MDJ.00	0.18	BO.YZK	4.0
BO.ISI	0.19	G.INU.00	3.7
BO.NAA	0.19	BO.TKD	3.6
IU.INCN.10	0.19	BO.SAG	3.5

Channels in the first column are with the lowest noise level (i.e., the standard deviation in the 10 min long time window preceding the earthquake). Channels in the third column are with the highest signal-to-noise ratio (SNR). We define SNR as the ratio of the expected prompt elastogravity signals (PEGS) amplitude at  $P$ -wave arrival time (computed with the Global Centroid Moment Tensor [Global CMT] parameters) over the noise level.

The instability (in terms of  $\alpha$  and  $M_w$ ) observed between  $t = t_0 + 4$  min and  $t = t_0 + 6$  min is directly related to the poor sensitivity of PEGS to the global source duration (Zhang *et al.*, 2020). This is shown in Figure 6, in which we impose  $\tau_c = h_d = 70$  s (the Global CMT value). In this case, the inverted solution remains stable and close to the Global CMT one, both in terms of focal mechanism and moment magnitude. This can also be illustrated when comparing data and synthetics. In Figure 7, we show vertical broadband records at stations IC.MDJ and IU.ULN, along with PEGS synthetics corresponding to solutions inverted for several source half-durations  $h_d$ . For simplicity, we consider  $\tau_c = h_d$  to have STF's starting at the origin time. Although very short ( $h_d = 10$  s) and very long ( $h_d = 200$  s) earthquake durations are inconsistent with observations, solutions obtained for  $h_d = 50$  s and  $h_d = 70$  s exhibit similar residuals. These two solutions are in good agreement with the Global CMT

focal mechanism ( $\alpha = 0.93$ ) but have significant differences in terms of moment magnitude ( $M_w$  8.8 for  $h_d = 50$  s, and  $M_w$  9.2 for  $h_d = 70$  s). Such a difference arises from the triangular-shaped STF used during inversion; due to its faster onset, a short-duration STF is more efficient for PEGS generation than a longer STF. Thus, a short STF needs a smaller scaling factor (the inverted magnitude) to get PEGS of similar amplitudes, compared with a longer STF. If short durations are further associated with solutions with a larger dip (which are more efficient in terms of PEGS radiation, see Vallée and Juhel, 2019), moment magnitude can be even more underestimated. This behavior is observed at time  $t = t_0 + 5$  min in Figure 5.

As a summary to this section, PEGS inversion for moment tensor provides stable and reliable information when the rupture duration is imposed close to the actual value. In a real-time perspective in which the duration is unknown, the inversion still converges toward a good set of parameters at times  $t > t_0 + 6$  min, but the variability at earlier times is an indicator of the nonuniqueness of the solution. A conservative way to interpret Figure 5 is that PEGS require a minimal magnitude of  $M_w$  8.6 and a dip-slip mechanism striking north-northeast-south-southwest.

### Joint Use of Pegs and $W$ Phase for Early Source Characterization

In this section, we assess the benefit of using a joint data set combining PEGS and  $W$ -phase waveforms for a fast and reliable characterization of very large earthquakes. We consider the maximum time of five minutes after the earthquake origin time, such that the joint data set includes 89 PEGS channels and 94  $W$ -phase channels. The corresponding sensor locations are shown in Figure 4. At  $t = t_0 + 5$  min, the complete PEGS records are available up to the maximum epicentral distance of  $22.5^\circ$ . In contrast, the  $W$ -phase waveforms are limited to the first  $8.3^\circ$ , because the  $W$ -phase window has a duration of 180 s starting at the  $P$ -wave arrival. As described in the  $W$ -phase section, we also remove seismic records within  $3.5^\circ$  of epicentral distance to mitigate the impact of source finiteness and clipping issues.

We normalize separately the PEGS and  $W$ -phase data sets, by their respective overall data maximum. This ensures that PEGS and  $W$ -phase data sets have a similar importance during the inversion of the source parameters. The source inversion is conducted using the combined data set as described in the previous section, and the corresponding results are shown in Figure 8. The first  $W$ -phase channels are progressively added at  $t \sim t_0 + 4$  min after onset time. At that time, 66 PEGS channels are already available inside the data set ( $\alpha \sim 0.9$ ,  $M_w$  9.45, see Figs. 5 and 8). From that time, and with the inclusion of the subsequent  $W$ -phase and PEGS channels, the geometrical similarity always remains higher than  $\alpha = 0.9$ , and the moment magnitude converges toward  $M_w$  9.2 at  $t = t_0 + 5$  min. This stable behavior contrasts with Figure 5, in which

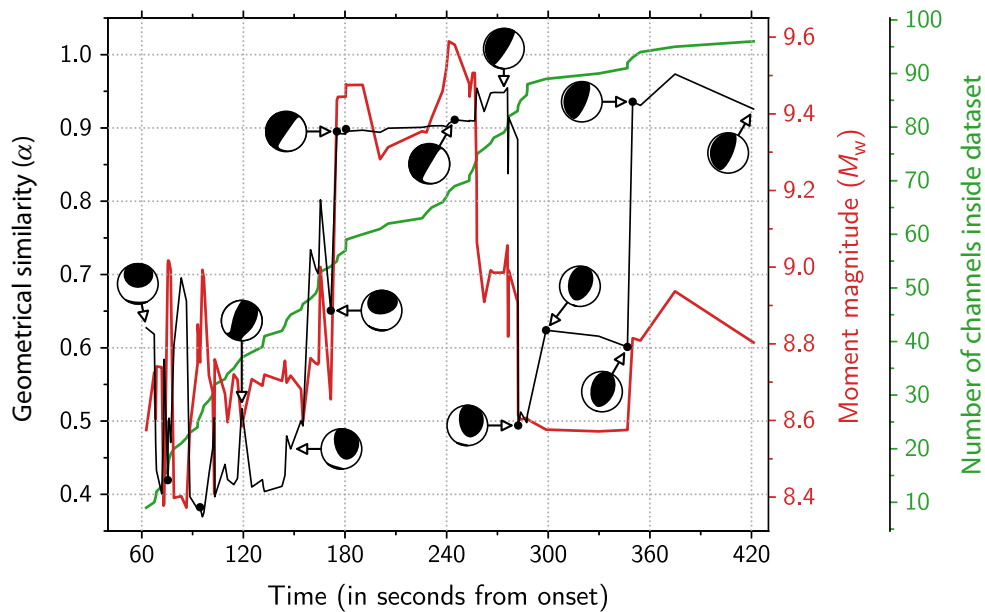


**Figure 5.** PEGS-based characterization of the Tohoku–Oki earthquake source parameters as time grows from origin time, and channels are added to the data set. The geometrical similarity  $\alpha$  (Rivera and Kanamori, 2014) of the inverted moment tensors compared with the Global CMT solution is shown in black and illustrated at representative times by their focal mechanism plots. A geometrical similarity  $\alpha$  close to 1 indicates a good agreement between focal mechanisms. The inverted moment magnitude and the number of channels inside the data set are shown in red and green, respectively. The black dots correspond to the inclusion of good-quality stations from the Vallée et al. (2017) data set. The color version of this figure is available only in the electronic edition.

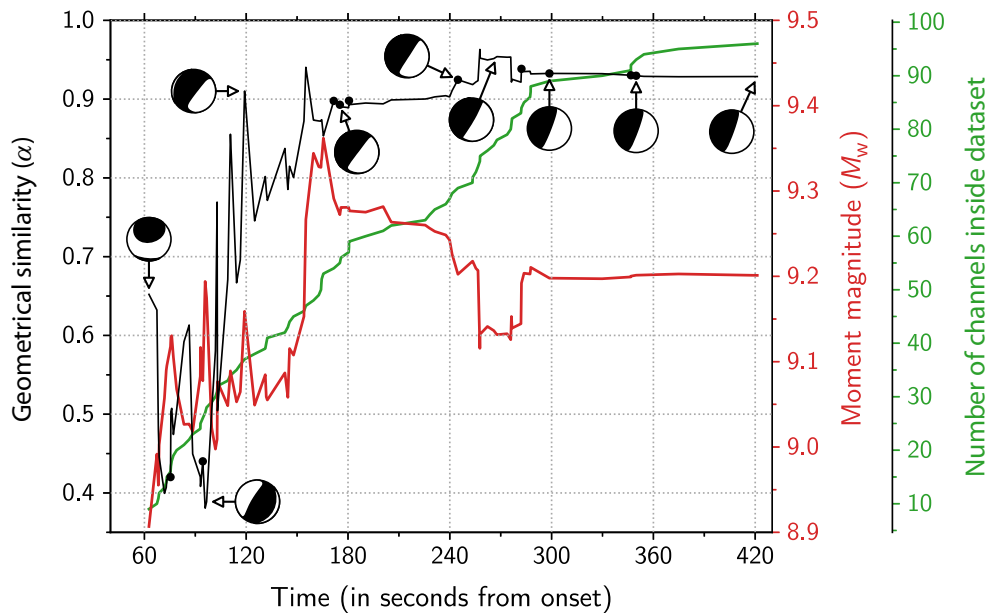


**Figure 6.** Same as Figure 5 but for  $\tau_c = h_d = 70$  s. The color version of this figure is available only in the electronic edition.

PEGS-based inversion exhibits a sudden change in the source parameters between  $t = t_0 + 4$  min and  $t = t_0 + 5$  min.

Another way to evaluate the impact of adding  $W$ -phase waveforms is by investigating the variability of the retrieved source models. With this purpose, we perform bootstrap (Tibshirani and Efron, 1993) with 1000 replications of the original data set, to assess the level of uncertainties at that time. At each replication, weights are randomly assigned to every channel in the data set (such that the sum of the random weights equals to the number of channels). The resulting probability density distributions for the moment magnitude  $M_w$  and the geometrical similarity  $\alpha$  are shown in Figure 9 at three different times: (1) at  $t = t_0 + 237$  s, just before the first inclusion of  $W$ -phase channels inside the joint data set; (2) at  $t = t_0 + 239$  s, after the addition of six  $W$ -phase channels from stations BO.SGN and BO.KMU (Fig. 4); and (3) at  $t \sim t_0 + 5$  min. As the data set grows, the scalar seismic moment distributions gradually shift toward the Global CMT solution ( $M_w$  9.08), and their standard deviation decreases. Interestingly, this effect is visible as soon as a few  $W$ -phase channels are included (case 2). The histograms for the geometrical similarity all have the maximum around  $\alpha \sim 0.9$ , but the tails of the distributions shrink with the number of channels inside the data set. As a consequence, when all  $W$ -phase channels have been included, solutions with  $\alpha < 0.8$  become very unlikely.



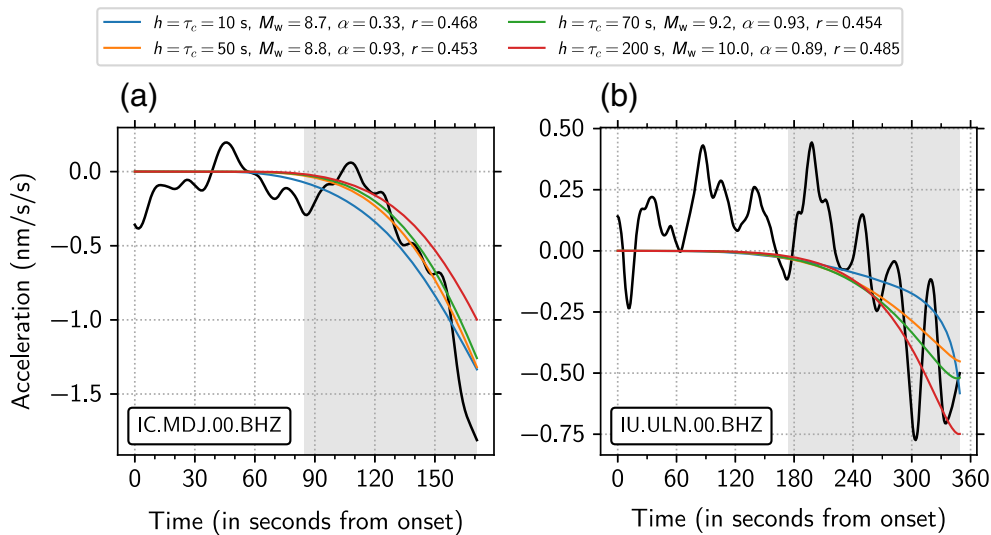


**Figure 7.** Vertical broadband records at (a) station IC.MDJ (location 00; in black) and (b) station IU.ULN (location 00; in black), and PEGS synthetics for a selection of source half-duration  $h_d$  and centroid time shift  $\tau_c$ , inverted at  $t = t_0 + 7$  min ( $n_{\text{cha}} = 96$  channels). The corresponding values of inversion residuals ( $r$ ), inverted moment magnitude ( $M_w$ ), and geometrical similarity ( $\alpha$ ) are shown in the top panel. The gray area, corresponding to  $(T_p/2, T_p)$ , in which  $T_p$  is the  $P$ -wave arrival time, represents the time window used during the inversion. The color version of this figure is available only in the electronic edition.

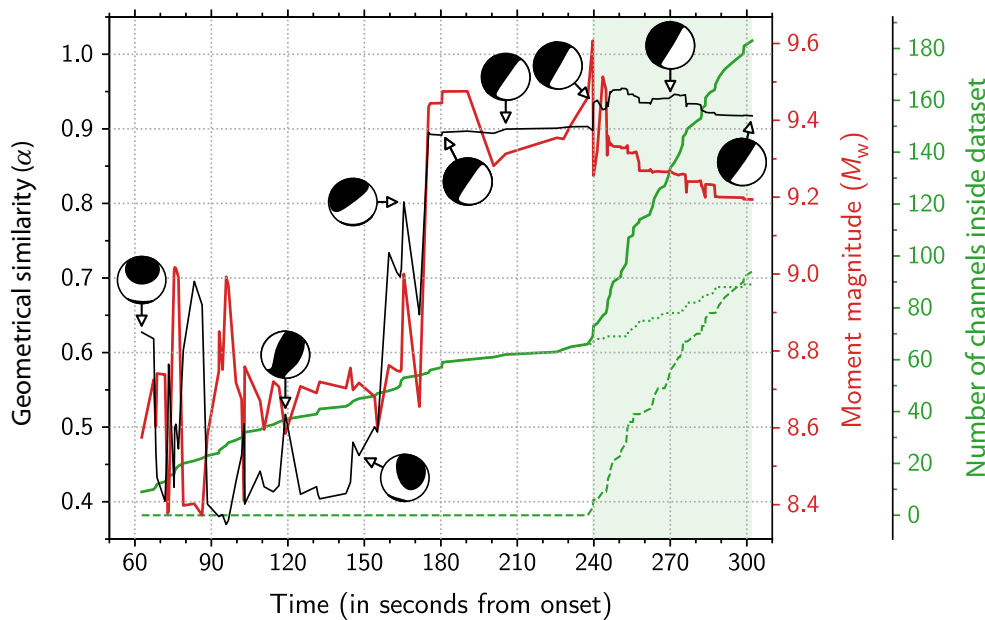


**Figure 8.** Joint inversion for the 2011 Tohoku–Oki earthquake source parameters, as time grows from source onset, and both PEGS and  $W$ -phase channels are added to the data set. The geometrical similarity  $\alpha$  (see Rivera and Kanamori, 2014, their equation 4) of the inverted moment tensors compared with the Global CMT solution is shown in black (illustrated at representative times by their focal mechanism plots), and the inverted moment magnitude is shown in red. The total number of channels inside the data set is depicted by the green solid line, separated into PEGS (dotted line) and  $W$ -phase channels (dashed line). The green area corresponds to the time at which  $W$ -phase channels are progressively added to the joint data set. The color version of this figure is available only in the electronic edition.

## Conclusion

Rapid earthquake characterization at regional distances is commonly based on seismograms windowed after the  $P$ -wave arrival. In the context of the 2011 Tohoku–Oki earthquake, we confirm here that the well-established  $W$ -phase method is able to provide a stable solution in less than 10 min after earthquake origin time. In the objective of an even earlier determination, we have explored the potential of the recently observed PEGS, which takes place between origin time and  $P$ -wave arrival. Moment tensor inversion of PEGS alone highlights their sensitivity to the focal mechanism type and their ability to provide a lower bound of the seismic moment. Starting from 3 min after the origin time, all inverted moment tensors consistently show a moment magnitude above 8.6 and a dip-slip mechanism on a north-north-east–south-southwest-striking plane. However, in a near-real-time perspective (i.e., when only location and origin time is known), a more accurate determination may suffer from uncertainties. They mostly come from trade-offs between source duration, moment magnitude, and steepness of the fault dip.

We show that an efficient way to reduce these trade-offs and the associated instability is the inclusion of early  $W$ -phase signals. In the 5 min following a large earthquake, we can gather PEGS up to an epicentral distance of  $22^\circ$  and  $W$ -phase signals up to an epicentral distance of  $8^\circ$ . As shown in Figure 8, this joint data set enables to stabilize the solution close to the Global CMT

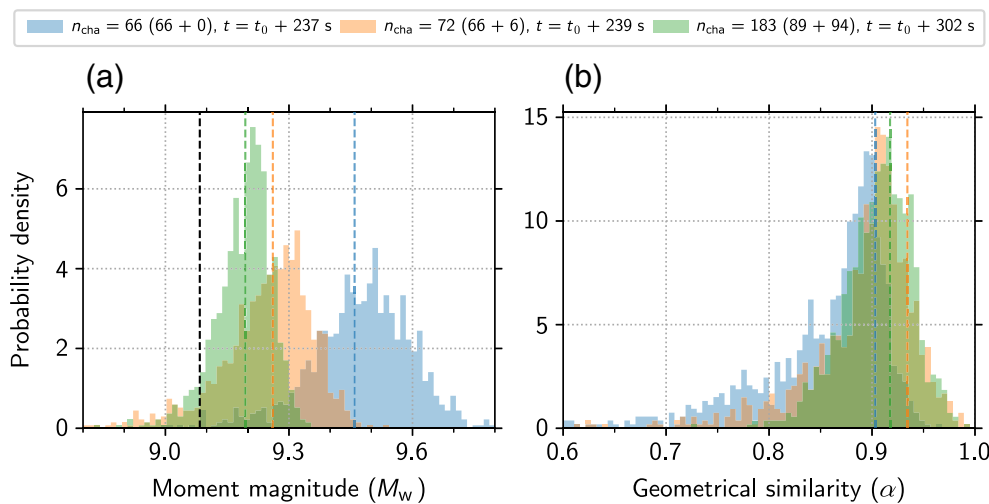


**Figure 9.** (a) Probability density distributions of moment magnitude  $M_w$  and (b) geometrical similarity  $\alpha$  to the Global CMT solution for the Tohoku–Oki earthquake, corresponding to 1000 bootstrap replications of linear inversions at three different times. The blue histograms result from the inversion of 66 PEGS channels at  $t = t_0 + 237$  s, the orange histograms from the joint inversion of 66 PEGS channels and six  $W$ -phase channels at  $t = t_0 + 239$  s, and the green histograms from the inversion of the entire data set at  $t \sim t_0 + 5$  min ( $n_{\text{cha}} = 183$ , separated into 89 PEGS and 94  $W$ -phase channels). The dashed colored lines highlight the solutions related to equal bootstrap weights across the considered data sets (data from all channels has a relative weight of 1) and correspond to solutions shown in Figure 8. The black dashed line corresponds to Global CMT solution for the Tohoku–Oki moment magnitude. The color version of this figure is available only in the electronic edition.

parameters of the Tohoku–Oki earthquake. Interestingly, in the context of areas less instrumented than Japan, even a few  $W$ -phase signals have a very positive effect on the solution (Fig. 9).

In addition to the combination with early  $W$ -phase signals, PEGS-based inversions would benefit from any approach improving their SNR. Based on the noise levels and PEGS amplitudes displayed in Figure 7, it is clear that part of the uncertainty affecting PEGS inversions is related to the noise level that makes different source scenarios difficult to distinguish. Promising approaches based on neural networks (e.g., denoising autoencoders) could mitigate noise effects and result in PEGS with higher SNRs. If such progress can be achieved, joint moment tensor inversions could then be conducted on other events reported in Vallée and Juhel (2019), such as the 2010  $M_w$  8.8 Maule earthquake (which suffered from a less instrumented area and noisier time series) or the 2018  $M_w$  7.9 Gulf of Alaska earthquake (for which relatively low magnitude is counterbalanced by the high-quality coverage of the USArray network).

## Data and Resources

Data from the following networks were used in this study (alphabetic order): National Research Institute for Earth Science and Disaster Prevention (NIED) F-net Network (BO), GEOFON Network (GE) available at doi: [10.14470/TR560404](https://doi.org/10.14470/TR560404), GEOSCOPE Network (G) available at

doi: [10.18715/geoscope.g](https://doi.org/10.18715/geoscope.g), the Hong Kong Seismograph Network (HK), the New China Digital Seismograph Network (IC) available at doi: [10.7914/sn/ic](https://doi.org/10.7914/sn/ic), the Global Seismograph Network (II) available at doi: [10.7914/sn/ii](https://doi.org/10.7914/sn/ii), the Global Seismograph Network (IU) available at doi: [10.7914/sn/iu](https://doi.org/10.7914/sn/iu), the Pacific21 network (PS, Earthquake Research Institute [ERI]), the Broadband Array in Taiwan for Seismology (TW) available at doi: [10.7914/SN/TW](https://doi.org/10.7914/SN/TW) the Northeast China Extended Seismic Array (YP) available at doi: [10.7914/sn/yp\\_2009](https://doi.org/10.7914/sn/yp_2009). Data were publicly accessed from the NIED data center available at <https://www.fnet.bosai.go.jp> for the F-net network and from the data center of Incorporated Research Institutions for Seismology (IRIS)-Seismological Facility for the Advancement of Geoscience (SAGE) available at <http://ds.iris.edu/ds/nodes/dmc/> for the other networks. NumPy (Harris et al., 2020) and scikit-learn (Pedregosa et al., 2011) were used to perform the source inversions,

Cartopy (Met Office, 2015), and Matplotlib (Hunter, 2007) for plotting purposes. All websites were last accessed in March 2023. The supplemental material includes an investigation of the inversion’s sensitivity to the centroid location and the source time function (STF) parameters, and a description of the criteria controlling the solution selection.

## Declaration of Competing Interests

The authors acknowledge that there are no conflicts of interest recorded.

## Acknowledgments

The authors thank the editor and two anonymous reviewers for their constructive comments and suggestions. The authors thank Rongjiang Wang for his open-source QSSP algorithm used to compute prompt elastogravity signal (PEGS) synthetics and Antoine Mocquet for fruitful discussions on moment tensor inversion. Kévin Juhel and Zacharie Duputel received funding from the European Research Council (ERC) under the European Union’s Horizon 2020 research and innovation program (Grant Agreements 949221 and 805256). Numerical computations were partly performed on the S-CAPAD/DANTE platform, Institut de physique du globe de Paris (IPGP), France.

## References

Albuquerque Seismological Laboratory/U.S. Geological Survey (2014). Global seismograph network (GSN), IRIS/USGS, available at <https://www.usgs.gov/programs/earthquake-hazards/gsn-global-seismographic-network> (last accessed October 2023).

- Colombelli, S., R. M. Allen, and A. Zollo (2013). Application of real-time GPS to earthquake early warning in subduction and strike-slip environments, *J. Geophys. Res.* **118**, no. 7, 3448–3461.
- Delouis, B. (2014). FMNEAR: Determination of focal mechanism and first estimate of rupture directivity using near-source records and a linear distribution of point sources, *Bull. Seismol. Soc. Am.* **104**, no. 3, 1479–1500.
- Duputel, Z., L. Rivera, H. Kanamori, and G. Hayes (2012). W phase source inversion for moderate to large earthquakes (1990–2010), *Geophys. J. Int.* **189**, no. 2, 1125–1147.
- Duputel, Z., L. Rivera, H. Kanamori, G. Hayes, B. Hirsorn, and S. Weinstein (2011). Real-time W phase inversion during the 2011 Tohoku-Oki earthquake, *Earth Planets Space* **63**, no. 7, 535–539.
- Dziewonski, A. M., and D. L. Anderson (1981). Preliminary reference Earth model, *Phys. Earth Planet. In.* **25**, no. 4, 297–356.
- Harris, C. R., K. J. Millman, S. J. Van der Walt, R. Gommers, P. Virtanen, D. Cournapeau, E. Wieser, J. Taylor, S. Berg, N. J. Smith, *et al.* (2020). Array programming with NumPy, *Nature* **585**, no. 7825, 357–362.
- Hayes, G. P., P. S. Earle, H. M. Benz, D. J. Wald, and R. W. Briggs (2011). 88 Hours: The US Geological Survey national earthquake information center response to the 11 March 2011 Mw 9.0 Tohoku earthquake, *Seismol. Res. Lett.* **82**, no. 4, 481–493.
- Hayes, G. P., L. Rivera, and H. Kanamori (2009). Source inversion of the W-phase: Real-time implementation and extension to low magnitudes, *Seismol. Res. Lett.* **80**, no. 5, 817–822.
- Hunter, J. D. (2007). Matplotlib: A 2D graphics environment, *Comput. Sci. Eng.* **9**, no. 3, 90–95.
- Institut de physique du globe de Paris (IPGP) and École et Observatoire des Sciences de la Terre de Strasbourg (EOST) (1982). GEOSCOPE, French Global Network of broadband seismic stations, available at <https://www.ipgp.fr/> (last accessed October 2023).
- Juhel, K., J.-P. Montagner, M. Vallée, J.-P. Ampuero, M. Barsuglia, P. Bernard, E. Clévéde, J. Harms, and B. F. Whiting (2019). Normal mode simulation of prompt elastogravity signals induced by an earthquake rupture, *Geophys. J. Int.* **216**, 935–947.
- Kanamori, H. (1993). W phase, *Geophys. Res. Lett.* **20**, no. 16, 1691–1694.
- Kanamori, H., and L. Rivera (2008). Source inversion of W phase: Speeding up seismic tsunami warning, *Geophys. J. Int.* **175**, no. 1, 222–238.
- Kikuchi, M., and H. Kanamori (1991). Inversion of complex body waves—III, *Bull. Seismol. Soc. Am.* **81**, no. 6, 2335–2350.
- Kimura, M., N. Kame, S. Watada, A. Araya, T. Kunugi, and R. Wang (2021). Determination of the source parameters of the 2011 Tohoku-Oki earthquake from three-component pre-P gravity signals recorded by dense arrays in Japan, *Earth Planets Space* **73**, no. 1, 223.
- Licciardi, A., Q. Bletery, B. Rouet-Leduc, J.-P. Ampuero, and K. Juhel (2022). Instantaneous tracking of earthquake growth with elastogravity signals, *Nature* **606**, no. 7913, 319–324.
- Met Office (2015). *Cartopy: A Cartographic Python Library With a Matplotlib Interface*, Met Office, Exeter, Devon.
- Minson, S. E., J. R. Murray, J. O. Langbein, and J. S. Gombert (2014). Real-time inversions for finite fault slip models and rupture geometry based on high-rate GPS data, *J. Geophys. Res.* **119**, no. 4, 3201–3231.
- Morales-Yáñez, C., Z. Duputel, and L. Rivera (2020). Impact of 3-D Earth structure on W-phase CMT parameters, *Geophys. J. Int.* **223**, no. 2, 1432–1445.
- Pedregosa, F., G. Varoquaux, A. Gramfort, V. Michel, B. Thirion, O. Grisel, M. Blondel, P. Prettenhofer, R. Weiss, V. Dubourg, *et al.* (2011). Scikit-learn: Machine learning in Python, *J. Machine Learn. Res.* **12**, 2825–2830.
- Riquelme, S., F. Bravo, D. Melgar, R. Benavente, J. Geng, S. Barrientos, and J. Campos (2016). W phase source inversion using high-rate regional GPS data for large earthquakes, *Geophys. Res. Lett.* **43**, no. 7, 3178–3185.
- Rivera, L., and H. Kanamori (2014). Diagnosing source geometrical complexity of large earthquakes, *Pure Appl. Geophys.* **171**, 2819–2840.
- Scripps Institution of Oceanography (1986). Global seismograph network, *IRIS/IDA*, available at <https://ida.ucsd.edu/> (last accessed October 2023).
- Tibshirani, R. J., and B. Efron (1993). *An Introduction to the Bootstrap*, Vol. 15, Monographs on statistics and applied probability, Chapman and Hall, New York.
- Vallée, M., J.-P. Ampuero, K. Juhel, P. Bernard, J.-P. Montagner, and M. Barsuglia (2017). Observations and modeling of the elastogravity signals preceding direct seismic waves, *Science* **358**, 1164–1168.
- Vallée, M., and K. Juhel (2019). Multiple observations of the prompt elastogravity signals heralding direct seismic waves, *J. Geophys. Res.* **124**, no. 3, 2970–2989.
- Wang, D., N. C. Becker, D. Walsh, G. J. Fryer, S. A. Weinstein, C. S. McCreery, V. Sardiña, V. Hsu, B. F. Hirshorn, G. P. Hayes, *et al.* (2012). Real-time forecasting of the April 11, 2012 Sumatra tsunami, *Geophys. Res. Lett.* **39**, no. 19, doi: [10.1029/2012GL053081](https://doi.org/10.1029/2012GL053081).
- Wang, R., S. Heimann, Y. Zhang, H. Wang, and T. Dahm (2017). Complete synthetic seismograms based on a spherical self-gravitating Earth model with an atmosphere–ocean–mantle–core structure, *Geophys. J. Int.* **210**, no. 3, 1739–1764.
- Zhang, S., R. Wang, T. Dahm, S. Zhou, and S. Heimann (2020). Prompt elasto-gravity signals (PEGS) and their potential use in modern seismology, *Earth Planet. Sci. Lett.* **536**, 116,150.

---

Manuscript received 21 June 2023

Published online 14 November 2023